Energy & Environmental Science

PAPER

View Article Online
View Journal | View Issue

Check for updates

Cite this: *Energy Environ. Sci.*, 2025, **18**, 4821

Advanced energy harvesting from low-frequency ocean waves for lithium-ion battery applications†

Yingjin Luo,[a] Wentao Lei,[a] Pengfei Chen,[b] Tao Jiang,[b] Andeng Liu,[a] Meidan Ye,[a] Zijie Xu,[b] Zhong Lin Wang*[b] and Wenxi Guo*[a]

Received 15th March 2025, Accepted 8th April 2025

DOI: 10.1039/d5ee01492a

rsc.li/ees

The low root mean square (RMS) current density generated by triboelectric nanogenerators (TENGs) has significantly hindered their effectiveness in charging lithium batteries. In response, we present a universal energy storage strategy for TENGs specifically designed for real marine environments, facilitating effective charging of lithium batteries for the first time. By integrating multiple grating electrodes and a ternary electrification architecture with an opposite-charge compensation mechanism, we increased the RMS current density of TENGs to 57.19 ± 0.23 mA m^{-2} Hz^{-1}. Additionally, we designed a lithium polymer charge management module that further boosts the RMS current density to 0.86 ± 0.02 A m^{-2} Hz^{-1}, a 14-fold improvement, enabling direct charging of 30 mA h and 40 mA h lithium batteries in 2.33 ± 0.05 h and 3.73 ± 0.14 h, respectively. Building on this foundation, we developed a self-powered remote (0.65 nautical miles) monitoring sensor network tailored for marine applications, enabling the initial use of Internet of Things technology in a marine environment.

Broader context

Triboelectric nanogenerators (TENGs), as a form of distributed energy harvesting technology, hold significant potential for improving the reliability of sensing systems in uninhabited and remote environments. However, the low root-mean-square (RMS) current density of TENGs has hampered their ability to effectively charge lithium batteries, thus limiting their practical applications. Here, we present a universal energy storage strategy for TENGs designed for real marine environments that achieves efficient charging of lithium batteries for the first time. By employing multiple grating electrodes and a ternary electrification architecture with an opposite-charge compensation mechanism, we have enhanced the RMS current density produced by a rotary triboelectric nanogenerator to 57.19 ± 0.23 mA m^{-2} Hz^{-1}. Subsequently, we design a Li-polymer charge management module that boosts the RMS current density to 0.86 ± 0.02 A m^{-2} Hz^{-1}, a 14-fold enhancement, enabling the direct charging of 30 mA h and 40 mA h lithium batteries within 2.33 ± 0.05 h and 3.73 ± 0.14 h, respectively. Furthermore, we have developed a self-powered, long-range (0.65 nautical miles) real-time environmental monitoring system specifically designed for marine environments, enabling wireless acquisition and transmission of offshore environmental data. This work presents a reliable strategy for energy storage in lithium batteries using TENGs and offers a promising solution for self-powered marine Internet of Things systems.

Introduction

To date, humans have been increasingly exploring and conquering the mysterious ocean, with the development of ocean energy primarily focusing on tidal energy, wave energy, and ocean thermal energy.[1–3] According to the International Energy Agency (IEA), the global potential for wave energy is estimated to be approximately 29 500 gigawatts. Concurrently, a substantial amount of energy can be harnessed from the expansive ocean to support diverse applications, including communication, monitoring, aquaculture, resource extraction, and corrosion protection.[4–6] Therefore, developing efficient and cost-effective strategies for harnessing and storing ocean energy, and applying it across various domains of marine development, is a critical issue for advancing sustainable human progress.[7–10] Nevertheless, the harsh and expansive characteristics of the environment frequently constrain the lifespan and operational range of monitoring equipment that heavily depends on batteries and/or corded power supplies.[11,12] Consequently, the exploration of eco-friendly power supply technologies that harness distributed environmental energy has been recognized as a promising solution to address these limitations.[13–16] Wave energy, recognized as one of the cleanest and most renewable environmental

[a] Department of Physics, College of Physical Science and Technology, Fujian Provincial Key Laboratory for Soft Functional Materials Research, Xiamen University, Xiamen, Fujian, 361005, China. E-mail: wxguo@xmu.edu.cn
[b] Beijing Key Laboratory of Micro-Nano Energy and Sensor, Center for High-Entropy Energy and Systems, Beijing Institute of Nanoenergy and Nanosystems, Chinese Academy of Sciences, Beijing, 101400, P. R. China. E-mail: zhong.wang@mse.gatech.edu

† Electronic supplementary information (ESI) available. See DOI: https://doi.org/10.1039/d5ee01492a

energy sources, presents an excellent solution for powering distributed sensors due to its high energy density and extensive availability.[17–22] Therefore, numerous technologies have been proposed to convert wave energy into electricity through various principles, including electromagnetic, piezoelectric, and triboelectric ones.[23–26] Triboelectric nanogenerators (TENGs) represent an effective device for converting high entropy energy into electricity, owing to their unique advantages of low manufacturing costs, high efficiency, and elevated power density.[27,28]

The application of TENGs for harvesting distributed energy has garnered significant interest over the past few decades.[29–33] However, in a low-frequency (<5 Hz) marine environment, due to the large intrinsic matching impedance (MΩ–GΩ) of TENGs, their high output voltage (kV) and low current (nA–μA), especially the RMS current usually in the order of μA (<10 μA), make it difficult to directly drive electronic devices or supply energy to a storage device.[34–36] Hence, the current mainstream energy storage strategies of TENGs employ capacitors as energy storage units.[37] Compared with conventional energy storage strategies, such as lithium batteries, capacitor storage has a lower energy density at the same voltage.[38] Furthermore, a capacitor itself suffers from fast charge release and short charge retention time, restricting its prolific extensive utilization as a universal energy storage device, and posing a significant challenge for the application of TENGs that employ this energy storage in real environments (oceans, lakes, deserts, *etc.*).[39,40] As such, it is essential to explore a universal high energy density energy storage strategy in the field of TENG energy harvesting.

In this work, a universal lithium battery energy storage strategy based on a rotating-mode triboelectric nanogenerator (RO-TENG) in a real ocean environment was designed and proposed. The RO-TENG relies on a gearbox to convert low-frequency wave excitation into low-torque, high-frequency rotational excitation and combines multiple grating electrodes and the opposite charge compensation mechanism to effectively harvest wave energy. The RMS current of the RO-TENG was measured to be 57.19 ± 0.23 mA m^{-2} Hz^{-1}, and a high average power density of 3.28 ± 0.07 W m^{-2} Hz^{-1} was recorded, corresponding to an intrinsic matching resistance of only 200 kΩ. This implies that significant progress has been made compared to previous efforts at an excitation frequency of 1 Hz. Meanwhile, after 48 612 960 cycles of stability testing, the RO-TENG demonstrates excellent durability, with an attenuation of only 10%. The RO-TENG establishes a robust and versatile foundation for the acquisition and conversion of ocean wave energy, which is crucial for optimizing the Li-polymer charge management system based on TENGs.

Subsequently, based on exceptional electrical performance, a Li-polymer charge management module (LPCMM), relying on a transformer circuit, and an under-voltage lockout (UVLO) circuit, was designed. An RMS current density of 0.86 ± 0.02 A m^{-2} Hz^{-1} is generated by the LPCMM-integrated parallel RO-TENG, representing a 14-fold enhancement. At the same time, when charged by the RO-TENG with the LPCMM operating at a frequency of 1 Hz for 1 h, the lithium battery's capacity increases to approximately 12 mA h, demonstrating an enhancement of more than 20 times compared to that of direct charging using a TENG. Furthermore, it takes 2.33 ± 0.05 h and 3.73 ± 0.14 h to fully charge lithium batteries with capacities of 30 mA h and 40 mA h, respectively. Moreover, when compared to the commercial charging method (LRH-250R), the RO-TENG method exhibits a charging time that is approximately 8% longer for achieving a full charge. Obviously, this demonstrates that this energy storage strategy has the potential for large-scale cascading applications.

Eventually, to demonstrate RO-TENG's potential for applications, it is utilized to directly power a 4×5 Bluetooth thermo-hygrometer array (a single sensor having a rated power consumption of 45 mW) with the assistance of the LPCMM. The networking of this sensor is also achieved to synchronize the temperature and humidity data back to the cloud in real time. On the other hand, a small self-powered marine environment monitoring system is developed to further verify the application capability of the RO-TENG. The remote real-time wireless (communication distances of 0.22 nautical miles and 0.65 nautical miles) monitoring of temperature, humidity, atmospheric pressure, and CO_2 levels, under the actual wave height ranging from 0.1 m to 0.3 m, is achieved. Overall, this work presents a reliable strategy for TENGs to store energy in lithium batteries, offering significant applications in distributed energy harvesting, self-powered intelligent networking, and regional environmental monitoring.

Results and discussion

Configuration and the working mechanism of the RO-TENG

The overall structure of the rotating-type TENG (RO-TENG) is schematically illustrated in Fig. 1(a), with the physical model presented in Fig. S1 (ESI†). The RO-TENG consists of two main components: a rotor and a stator. The rotor, made of an acrylic material, features four symmetrically arranged weights of equal mass on its upper surface and 60 fan-shaped polytetrafluoroethylene (PTFE) films on its lower surface, each with a central angle of 3°. Conversely, the stator, also constructed from an acrylic material, is equipped with 120 nylon-coated copper electrodes, which are similarly arranged with the same central angle on its upper surface. This design integrates multiple tunnels and grating electrodes to enhance electrostatic induction and current output (Fig. 1(b)). On the other hand, to minimize contact friction and wear, the two tribo-materials are maintained at a fixed distance, with an air gap of 0.5 mm, thus establishing a non-contact mode structure. However, this non-contact configuration reduces the charge transfer efficiency between the tribo-layers, and the rapid decay of pre-existing charges on both triboelectric layers results in a continuous decrease in the electric output during prolonged operation. To address these challenges, a narrow slot has been machined to accommodate a single rabbit fur brush of equivalent dimensions. This brush is intended to enhance the surface charge density of the tribo-layers, thereby preserving the triboelectric charges on the material surfaces while maintaining a fixed distance in the non-contact mode structure (Fig. 1(c)).

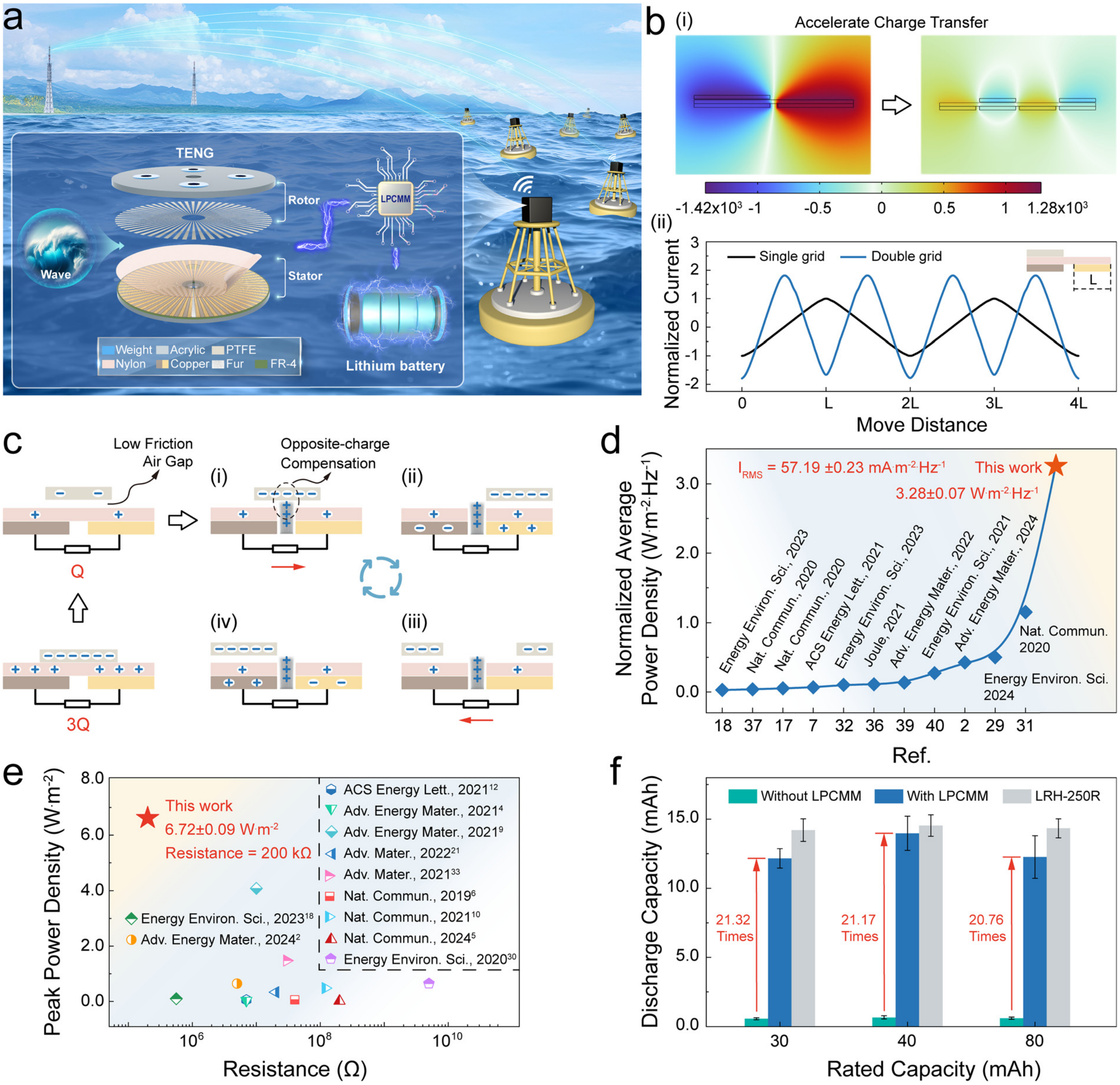

Fig. 1 Schematic structure and working principle of the RO-TENG. (a) Structure scheme of the MO-TENG. (b) Simulation results for the optimization of the grating, including (i) grating potential distribution and (ii) current density. (c) Optimized contact mode of the TENG and a corresponding schematic diagram illustrating its operating principle. (d) Comparison of the average power output of the RO-TENG with other related works. (e) Comparison of the peak power and optimal resistance of the RO-TENG with various designs. (f) Comparison of the discharge capacity of lithium batteries charged for 1 h using the RO-TENG with and without the LPCMM, and the commercial method (LRH-250R).

Stages (i)–(iv) in Fig. 1(c) illustrate the charge flow across the external circuit. Initially, the rotor is charged through rotary triboelectrification with PTFE. Subsequently, the relative motion between the rotor and stator induces the migration of free electrons between the two electrodes on the stator due to electrostatic induction, generating alternating current. In summary, owing to the incorporation of multiple grating electrodes and a ternary electrification architecture featuring an opposite-charge compensation mechanism, the RO-TENG ensures both high-performance output and long-term operational stability.

Power density and long-term operational stability are critical fundamental parameters that serve as key indicators for evaluating the performance of TENGs. Regarding power density, the normalized average power density (P_{norm}) emerges as an essential metric, depending on three primary factors: current (I), resistance (R), and, area (A), as described in eqn (1).

$$P_{\mathrm{norm}} = \frac{P_{\mathrm{ave}}}{A} = \frac{\int_0^T I(t)^2 R\mathrm{d}t}{T \cdot A} \tag{1}$$

where $I(t)$ represents the current across the resistor at the time t, R is the resistance, T is the integration time, and A is the area of the TENG. Given the pulsed nature of the current (I) generated by the TENG, the root-mean-square (RMS) current (I_{RMS}) becomes crucial for accurately determining P_{norm}. In addition, regarding the resistance (R), the commonly used matching resistance at the MΩ level should be reduced to the kΩ or Ω level for practical applications, in accordance with impedance matching principles. This adjustment implies that, for a specified unit area, R should be minimized while simultaneously maximizing I_{RMS} to achieve a higher P_{norm}. Consequently, a comprehensive measurement approach encompassing four parameters based on average power density, RMS current density, matching resistance and long-term operation stability is proposed, as illustrated in Fig. S2 (ESI†).

The current generated by the TENG in response to stochastic environmental stimuli, such as the triggering by an ocean wave, exhibits a pulsed character, leading to a low effective current (RMS current). To enhance the RMS current of the RO-TENG, a gearbox is employed to convert heaving motion of the wave into unidirectional rotation of the rotor. This conversion allows for the sustained generation of current from a single trigger of an ocean wave. The detailed working process of the RO-TENG is documented in Note S1 (ESI†). Meanwhile, the rotor electrodes consist of 60 fan-shaped polytetrafluoroethylene (PTFE) films, each with a central angle of 3°, which are fabricated using laser cutting technology. Due to refining of electrodes, this approach significantly reduces the transit time for charge movement between the electrodes. Furthermore, the combination of PTFE and rabbit fur, which exhibit opposite charge polarities, contributes to a ternary electrification architecture (PTFE, rabbit fur, and nylon). This design effectively increases the charge transfer between the electrodes. As a result of these innovations, the RMS current density and average power density of the RO-TENG have been measured at 57.19 ± 0.23 mA m^{-2} Hz^{-1} and 3.28 ± 0.07 W m^{-2} Hz^{-1}, respectively, representing a remarkable increase compared to those reported in previous related work (Fig. 1(d) and Fig. S2(i), (ii), Table S1 (ESI†)).

In addition, due to the refinement of the RO-TENG's grid, it has a small internal resistance (a matching resistance of 200 kΩ) and can produce a much larger peak power density (6.72 ± 0.09 W m^{-2}), compared to previous studies (Fig. S2(iv) (ESI†) and Fig. 1(e)). On the other hand, the wear of triboelectric materials has consistently posed a significant challenge in the long-term operation of TENGs for wave energy harvesting in natural environments. In comparison to current best work, the RO-TENG, which is based on a ternary electrification architecture, demonstrates exceptional long-term operational stability, exhibiting only a 10% reduction in performance after over 48 million continuous cycles, with the stability/decay value being 6.13 times that of previous systems (Fig. S2(iii) and S3 (ESI†)). Subsequently, representative data from the discharge capacity of the lithium battery charged by the RO-TENG without and with LPCMM and LRH-250R were collected and analyzed, and the results are presented in Fig. 1(f). Notably, when the lithium battery is charged by the RO-TENG with the LPCMM operating at a frequency of 1 Hz for 1 h, its capacity increases to approximately 12 mA h, indicating an improvement of over 20-times compared to direct TENG charging. Moreover, relative to the commercial charging method (LRH-250R), the RO-TENG method exhibits a charging time that is approximately 8% longer to achieve a full charge (see Fig. S4 (ESI†)). To put it briefly, benefiting from the enhanced performance of the RO-TENG in terms of RMS current density and average power density, the successful charging of commercial lithium batteries has been achieved, elevating TENGs to a new level of practical applications in natural environments.

Optimization of structural parameters of the RO-TENG

To ensure the effective operation of the RO-TENG in an ocean environment and to optimize its output performance, we investigated the contact torque between the rotor and rabbit fur, as well as the device's output performance under stable laboratory-controlled conditions. A standardized experimental platform was established to meet the requirements of these investigations, as schematically shown in Fig. S5 (ESI†). To closely simulate ocean wave excitation under natural conditions, the excitation frequency and stroke were configured at 1 Hz and 160 mm, respectively. Fig. 2(a) illustrates the impact of the distance between the rabbit fur and the stator surface (D_{RF}, as depicted in Fig. S6 (ESI†)) on both transfer charge and contact torque within the RO-TENG, with an air gap between the rotor and stator set at 0.5 mm. The data indicate that an increase in D_{RF} leads to a rise in both the output charge of the RO-TENG and the contact torque. This relationship arises because D_{RF} influences the contact force between the rotor and the rabbit fur. However, while an increase in contact torque may enhance output charge, it can also pose challenges to the operational viability of the device in an oceanic environment, as it requires greater driving force to operate effectively. Additionally, heightened contact torque can intensify the wear of triboelectric materials, thereby diminishing the electrical output of the RO-TENG during prolonged use. Consequently, the optimal D_{RF} for the rabbit fur was determined to be 1 mm when maintaining an air gap of 0.5 mm between the rotor and the stator.

Subsequently, we conduct a systematic analysis of the impact of the specific ratio between the area of rabbit fur and the area of Cu electrode of the stator (the area of rabbit fur/the area of the Cu electrode ($A_{\text{RF/Cu}}$), as illustrated in Fig. S7 (ESI†)) on performance of the RO-TENG, with an air gap and D_{RF} set at 0.5 mm and 1 mm, respectively. As depicted in Fig. 2(b), there is a positive correlation between $A_{\text{RF/Cu}}$, contact torque, and charge density of the RO-TENG. When $A_{\text{RF/Cu}}$ increases from 0 to 3.45%, the charge density rises from 6.46 ± 0.54 μC m^{-2} to 9.98 ± 0.53 μC m^{-2}, reflecting an improvement of over 30%. This increase can be attributed to the enlargement of the contact area between the rotor and the rabbit fur, which enhances charge transfer to the stator grid. Furthermore, the expansion of the contact area significantly increases the contact force between the rotor and rabbit fur, leading to a corresponding increase in contact torque. Specifically, contact torque increases from 11.57 ± 2.25 mN m to 60.03 ± 2.04 mN m, representing a growth of more than 80%. As previously analyzed in Fig. 2(a), the increase in contact torque may present operational reliability issues for the RO-TENG when it is deployed in natural environments over extended periods.

In addition to the effects of charge density and contact torque, we also investigated the influence of $A_{\text{RF/Cu}}$ on the

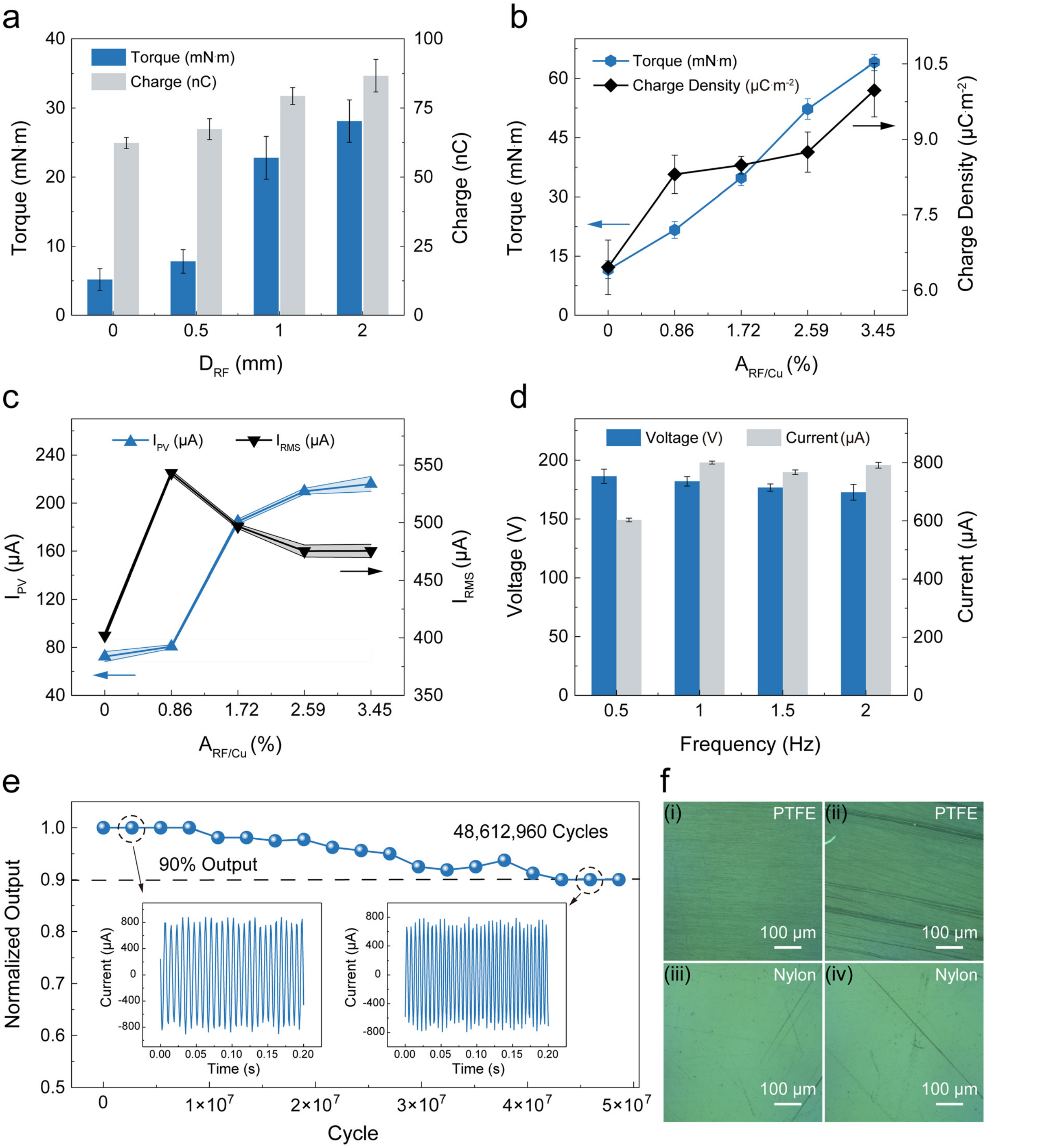

Fig. 2 Influences of materials on the performance of the RO-TENG. (a) Illustration of the variation in torque and transferred charge under different D_{RF}. (b) Torque and output charge density of the RO-TENG with different $A_{RF/Cu}$. (c) I_{PV} and I_{RMS} of the RO-TENG obtained using different $A_{RF/Cu}$. (d) Voltage and current outputs of the RO-TENG at various driving frequencies. (e) Durability test of the RO-TENG. (f) Comparison of the material abrasion of the RO-TENG after 72 h of continuous testing, (i) and (iii) before testing, (ii) and (iv) after testing.

current output of the RO-TENG. As a result of the contact torque, the output current of the RO-TENG demonstrates a periodic decay characteristic, as illustrated in Fig. S8–S12 (ESI†). The difference between the peak and valley values of the current (I_{PV}), along with the RMS current (I_{RMS}) for a single cycle, was selected to assess the influence of the RO-TENG's current under varying $A_{RF/Cu}$ conditions (Fig. 2(c)).

As the $A_{RF/Cu}$ increased, the charge density of the RO-TENG improved, resulting in a higher peak current. For instance, at an $A_{RF/Cu}$ of 0.86%, the peak current increased from

602.67 ± 6.43 μA to 800.33 ± 5.03 μA, marking a 25% enhancement (Fig. S8a and S12a (ESI†)). Similarly, I_{RMS} increased from 401.96 ± 2.96 μA to 543.25 ± 2.16 μA, reflecting a 26% improvement (Fig. S8b and S12b (ESI†)). However, when $A_{RF/Cu}$ increased from 0.86% to 3.45%, the peak current exhibited only a negligible additional increase (Fig. 2(c) and Fig. S8a, S12a (ESI†)). Notably, I_{PV} increased with the increase in $A_{RF/Cu}$ due to the augmented contact torque. This rise in I_{PV} intensified the fluctuations in the output current of the RO-TENG, leading to an unstable electrical energy output. The variation in I_{RMS} supports this conclusion, as it dropped from 543.25 ± 2.16 μA to 475.38 ± 5.67 μA when the $A_{RF/Cu}$ was increased to 3.45%, indicating a 12% decrease (Fig. 2(c) and Fig. S8b–S12b (ESI†)). Thus, to achieve stable electrical energy output, an $A_{RF/Cu}$ of 0.86% was chosen to maintain an adequate I_{RMS}.

Subsequently, we tested the output performance of the RO-TENG at various excitation frequencies, yielding an open-circuit voltage of 182.25 ± 4 V, a short-circuit current of 800.33 ± 5.03 μA, and a transferred charge of 68.36 ± 6.21 nC at the selected excitation frequency (Fig. 2(d) and Fig. S13 (ESI†)). The long-term durability test results of the RO-TENG are depicted in Fig. 2(e), showing that the normalized current maintains excellent electrical stability, retaining 90% of the initial output after 48 612 960 cycles (72 h). Observations under an optical microscope revealed the extent of material abrasion after 72 h of continuous testing (Fig. 2(f)). In summary, the RO-TENG demonstrates excellent long-term operational stability while maintaining high electrical output performance.

Li-polymer charge strategy for the RO-TENG

To enhance the energy storage efficiency and supply electronic circuits with applicable voltage, a universal Li-polymer charge management strategy relying on the RO-TENG and Li-polymer charge management mode (LPCMM) was developed, as depicted in Fig. 3(a). The LPCMM consists of a transformer circuit, a Li-polymer charge management circuit, and an under-voltage lockout (UVLO) circuit. Its output current variations on typical nodes are depicted in Fig. 3(b) and the photograph of the LPCMM is presented in Fig. 3(c).

The transformer circuit is built upon a transformer and a rectifier bridge (ABS210), which reduces the output voltage, enhances the current output from the RO-TENG, and converts AC to DC simultaneously (Fig. 3(b)-(i), (ii)). At a working frequency of 1 Hz, the maximum peak value of the output current after the transformer rises from 800.33 ± 5.03 μA to 12.27 ± 0.27 mA, while the output voltage drops from 182.25 ± 4 V to 7.33 ± 0.47 V (Fig. 3(d) and Fig. S14 (ESI†)). Additionally, the average and peak output power of the RO-TENG, both with and without the transformer, relative to load resistance is illustrated in Fig. 3(e) and Fig. S15 (ESI†). The black curve shows the average output power through the transformer, with a load resistance varying from 0.1 kΩ to 2.5 kΩ, reaching a maximum of 25.74 ± 0.57 mW at a load resistance of 400 Ω. In contrast, when the transformer is not used (shown by the blue curve), the maximum average output power is 31.11 ± 0.67 mW at a load resistance of 200 kΩ. The energy conversion efficiency achieved using this rectification circuit is 82.74%. Importantly, the matching impedance for the maximum power output has been reduced from 200 kΩ to 400 Ω, representing a remarkable decrease of 500 times, which is critical for optimizing the Li-polymer charge management system.

The Li-polymer charge management circuit was designed depending on a Li-polymer charge management controller (LPCMC). Lithium battery charging typically comprises four phases: the pre-charge phase, the constant-current (CC) phase, the constant-voltage (CV) phase, and the charge done. The LPCMC switches among these three phases by detecting the battery voltage. The pre-charge phase is employed for the restorative charging of a fully discharged battery, the voltage of which is lower than 3 V. Its charging current is one tenth of the constant-current charging current, that is, 0.1 C (The C-rate denotes the ratio between a battery's rated capacity and its charging or discharging current. For instance, if a battery has a rated capacity of 100 mA h, a C-rate of 1 C indicates that the charging current for this battery is 100 mA during the CC phase.). When the battery voltage exceeds the threshold of the pre-charge phase at 3 V, the charge current is enhanced to enter the CC phase. During the CC charging process, the current rises to the set current and remains constant. Meanwhile, the voltage will gradually ascend until reaching the threshold voltage, which is set at 3.7–4.2 V for a single battery. Until the battery voltage reaches the set voltage, the CC charging phase terminates and the CV phase commences. Throughout this process, the voltage remains constant, and the charging current is dependent on the saturation degree of the battery. As the charging process progresses, it gradually decreases from the maximum value. Finally, when the charging current reduces to 0.01 C, the charging process is considered terminated.

Fig. 3(f) illustrates the electrical output of the LPCMM with a single RO-TENG connected under no-load conditions. The output voltage is consistently maintained at 4.2 ± 0.01 V, while the output current exhibits a periodic waveform, with an RMS value of 8.21 ± 0.16 mA (Fig. S16 (ESI†)). In the CC charging phase of the lithium battery, as demonstrated in Fig. 3(g)–(i), the LPCMM successfully charges lithium batteries of 30 mA h, 40 mA h, and 80 mA h capacities to 3.5 V within 288 ± 4.73 s, 498 ± 10.58 s, and 767 ± 15.72 s, respectively (see Fig. S17 and Table S2 (ESI†)). Notably, owing to the enhanced stability and significantly higher charging current during the charging process of the 80 mA h lithium battery (Fig. 3(h)), the LPCMM achieved a 48.9 times improvement in the charging rate compared to systems not incorporating the LPCMM. Furthermore, the charging rate using the LPCMM is only 3.51% slower than that achieved by a commercial method (LRH-250R, as shown in Fig. 3(h) and Fig. S18, S19 (ESI†)). Subsequently, voltage–capacity data for lithium batteries of various rated capacities during the constant-current discharge process were recorded (Fig. 3(i)). After charging the batteries to 3.5 V, their effective capacities were found to be 0.54 ± 0.14 mA h, 0.91 ± 0.17 mA h, and 3.22 ± 0.23 mA h, respectively.

Additionally, to ensure complete self-powered functionality of the LPCMM, an under-voltage lockout (UVLO) circuit was

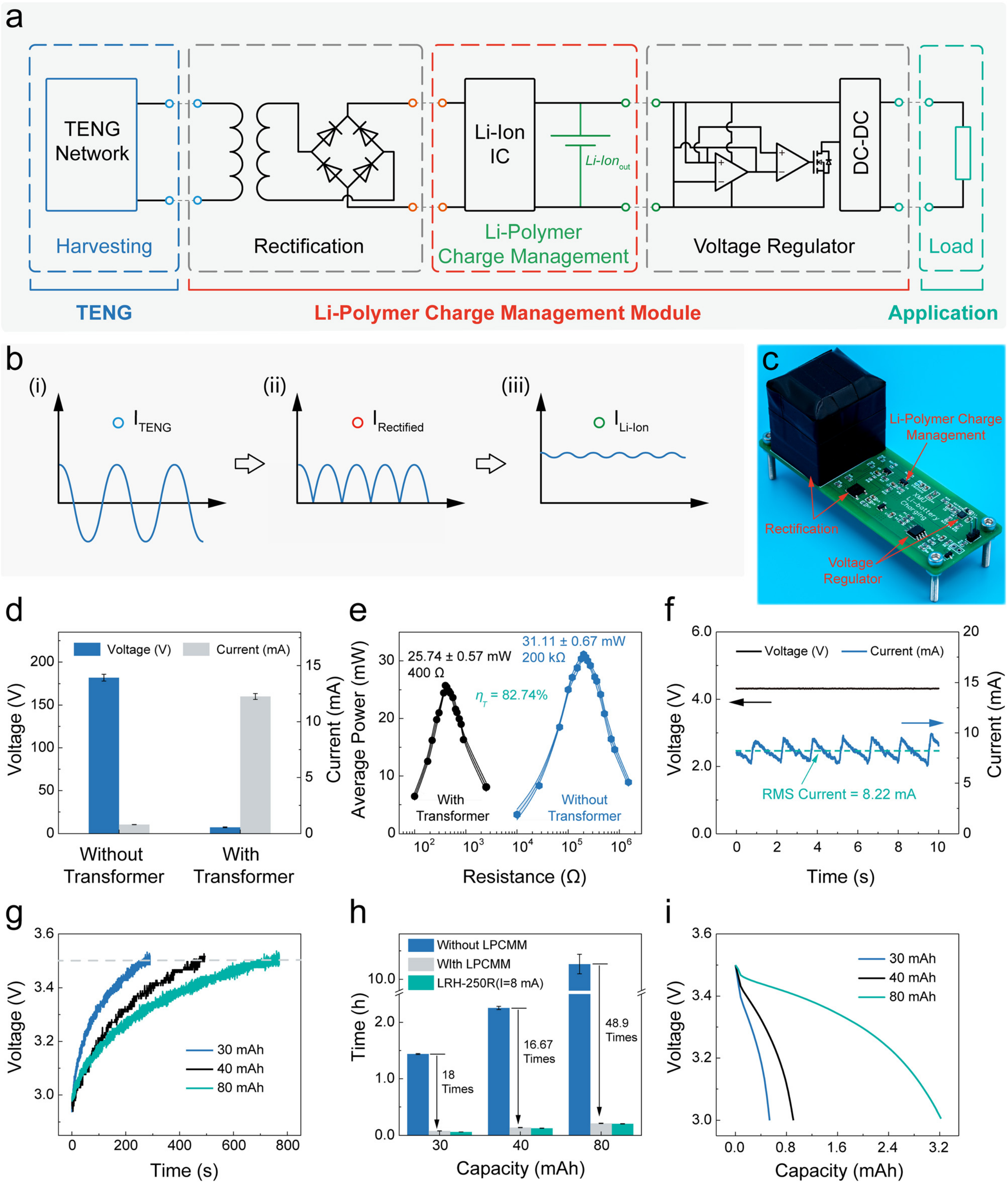

Fig. 3 Schematic design and performance evaluation of the Li-polymer charge management module (LPCMM) based on the RO-TENG. (a) Circuit diagram of the Li-polymer charge management circuit. (b) Illustration of the current variation on typical nodes of the LPCMM. (c) Photograph of the LPCMM. (d) Comparison of the output voltage and current of the RO-TENG with and without the transformer. (e) Comparison of average output power between the cases with and without the transformer unit. (f) Illustration of the voltage, current, and RMS current variation of LPCMM at an excitation frequency of 1 Hz. (g) Voltage curves for different capacities of lithium batteries at an excitation frequency of 1 Hz. (h) Charging time comparison between the RO-TENG with and without the LPCMM and LRH-250R, at a voltage range of 3 V to 3.5 V. (i) Variation curves of discharge voltage with capacity of lithium batteries with different capacities.

designed using an operational amplifier and a DC–DC power chip (TPS63900DSKR). When energy is harvested by the RO-TENG, the electricity can be extracted quickly to the lithium battery *via* a transformer circuit and a Li-polymer charge management circuit. Meanwhile, once the voltage of the lithium battery (V_{Store}) reaches 3.5 V, the constant-voltage at 3.3 V (V_{Load}) is exported by the UVLO. And as the energy of the V_{Store} is consumed, V_{Load} will be cut off through the UVLO, when the V_{Store} is lower than 3 V. Therefore, the V_{Load} is automatically controlled by the UVLO, demonstrating a completely self-powered functionality. The detailed circuit scheme, mechanism and component parameters can be found in Note S2 (ESI†), respectively.

To further demonstrate the charging capability of the LPCMM, a series of experiments were conducted using a parallel configuration of the rotary triboelectric nanogenerator (RO-TENG), with results illustrated in Fig. 4. The circuit diagram depicting the LPCMM connected to the parallel RO-TENG is shown in Fig. 4(a) and Fig. S20 (ESI†). Fig. 4(d) presents the peak current, peak power, and average power output of the parallel RO-TENG in relation to varying load resistances. At an excitation frequency of 1 Hz, the parallel RO-TENG achieves maximum average and peak power outputs of 66.14 $\pm$ 2.10 mW and 122.13 $\pm$ 2.02 mW, respectively, at a matched resistance of 120 kΩ. The charging performance of the LPCMM with the parallel RO-TENG configuration was then evaluated, as shown in Fig. 4(c)–(f). In a no-load condition, similar to the previous results (Fig. 3(f)), the output voltage of the system remained steady at 4.2 $\pm$ 0.01 V while the output current exhibited a periodic waveform, with an RMS current of 15.44 $\pm$ 0.51 mA approximately double that of a single RO-TENG (Fig. 4(c) and Fig. S21 (ESI†)). This increase in RMS current translates to a significantly enhanced charging rate for lithium batteries of equivalent capacity, with improvements of 222%, 192%, and 154%, respectively (Fig. 4(d)). Furthermore, when compared to the charging rates offered by the commercial LRH-250R (illustrated in Fig. S22 (ESI†)), the LPCMM integrated with the parallel RO-TENG closely matches the performance of the LRH-250R (Fig. 4(e)).

Following this, the entire charging process of various lithium batteries was measured and the results are illustrated in Fig. 4(f) and Fig. S23 (ESI†). Similar to the analysis presented in the previous section, the charging of the lithium batteries progresses through four distinct phases. Initially, when the voltage of the lithium battery is below 3 V, the system enters the pre-charge phase. As charging continues (as depicted in Fig. 4(f)-(i), (ii)), both the charging voltage and current rise. Once the voltage exceeds 3 V, the system transitions into the CC charging phase. During this phase, the charging current is maintained at 15 mA (corresponding to a charge rate of approximately 0.5 C to 0.4 C), while the voltage gradually increases. When the voltage reaches 4 V, the system enters the CV charging phase, during which the charging current gradually decreases and the voltage slowly rises to approximately 4.2 V, where it is held steady. The charging process concludes when the charging current drops to 0 mA (below 0.01 C). The LPCMM-integrated parallel RO-TENG required 2.33 h and 3.73 h to fully charge the 30 mA h and 40 mA h lithium batteries, respectively. Subsequently, we measured the voltage-capacity data of the lithium batteries during the constant-current discharge process (see Fig. S24 (ESI†)). The effective capacities recorded were 26.57 $\pm$ 0.35 mA h and 34.87 $\pm$ 0.38 mA h, which resulted in capacity achievement rates of 88.57% and 87.18%, respectively.

Additionally, to demonstrate the application capability of the entire system, a self-powered temperature–humidity wireless Bluetooth monitoring array was fabricated by integrating the RO-TENG, LPCMM, and 20 commercial Bluetooth thermo-hygrometers (Fig. 4(g)). An 80 mA h lithium battery is charged to 3.5 V after 420 s, at which point the thermo-hygrometer initiated its operation and continued to function autonomously. Even after excitation ceased, the thermo-hygrometer operated normally for 1 h. Successful wireless transmission of signals to a mobile phone was achieved through the Bluetooth Mesh network, as shown in Movie S1 (ESI†). Moreover, once excitation was reapplied, the system quickly resumed operation. This application exemplifies the exceptional performance of our system, which effectively integrates the RO-TENG with the LPCMM.

Application demonstration

The preceding studies demonstrated the exceptional performance of the practical applications developed. As a result, we conducted a series of experiments in the real ocean environment of Dali Puyu, Xiamen (188°9′23″ E, 24°33′11″ N, Fig. S25 (ESI†)), with the results presented in Fig. 5. We developed a self-powered wireless sensing node that utilizes a wave energy absorption device integrated with a sensing system, alongside a dedicated receiver terminal and display program. A compact experimental device employs a float to capture wave excitation in a 360-degree range, thereby driving the RO-TENG to convert wave energy into electrical power. Under various wave frequency conditions, the device is capable of operating effectively, as shown in Movies S2 and S3 (ESI†). As illustrated in Fig. S26 and Movie S4 (ESI†), 45 high-power LEDs are efficiently powered by this device, emitting bright light even during the daytime.

The sensing system consists of a LPCMM, a wireless MCU, and a sensing module, capable of measuring temperature, humidity, atmospheric pressure, and CO_2 levels. The wireless sensing node was placed in the location around the receiver, as shown in Fig. 5(a) and Fig. S27 (ESI†). The distances from the sensing node to receiver #1 and receiver #2 are 0.22 nautical miles (0.4 km) and 0.65 nautical miles (1.2 km), respectively. Photographs of the test site layout, the wireless sensing transmitter, and the receiver terminal are shown in Fig. 5(b)–(d), respectively. The circuit diagram of self-powered wireless sensing node is shown in Fig. 5(e). Detailed circuit schematic, mechanisms, and component parameters can be found in Table S3 (ESI†).

Fig. 5(f) illustrates a typical charging curve of a 40 mA h lithium battery utilizing the LPCMM-integrated parallel RO-

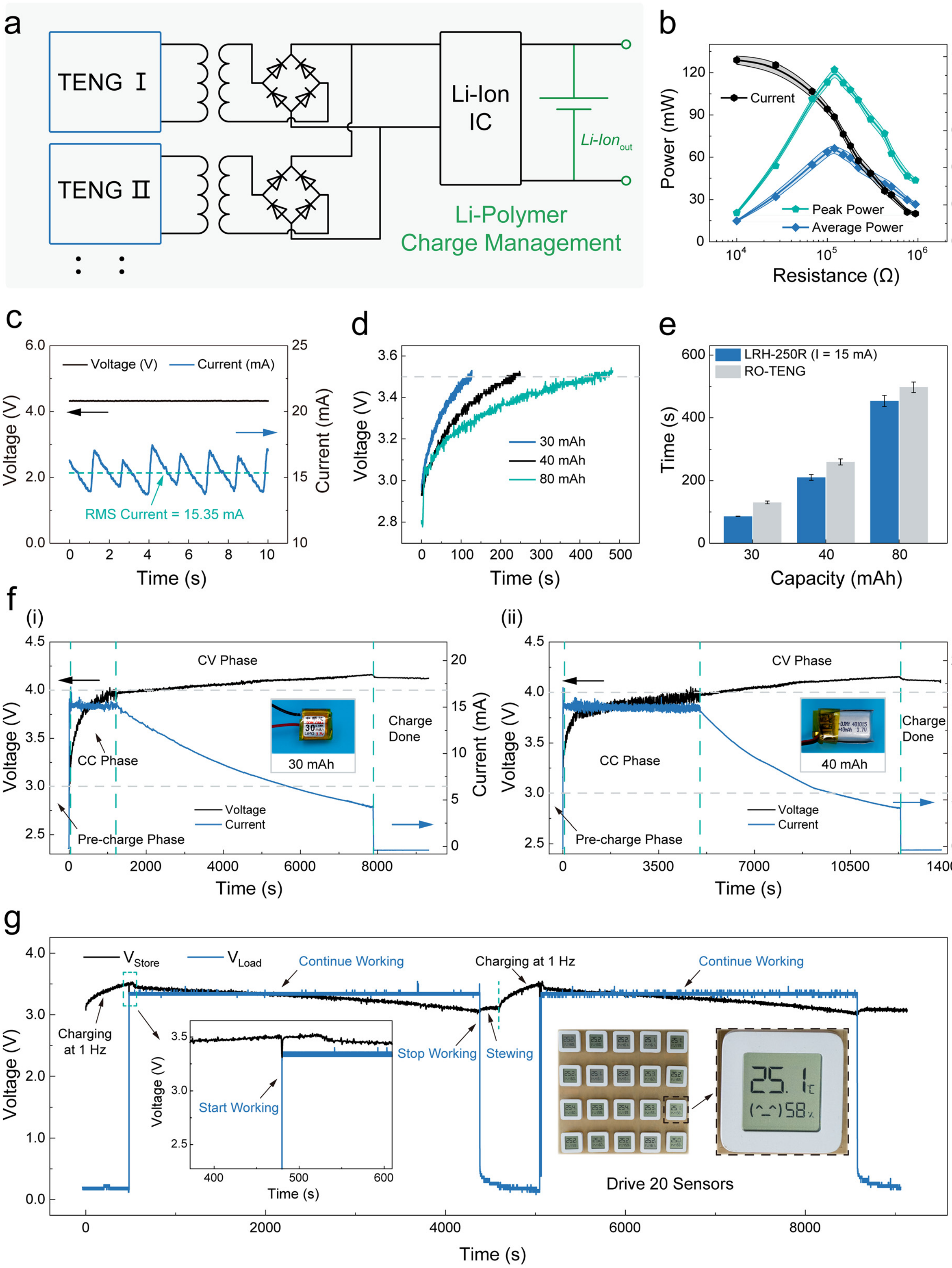

Fig. 4 Performance and application of the parallel RO-TENG devices. (a) Circuit diagram of the parallel RO-TENG connection with the LPCMM. (b) Illustration of output power under various load resistances using parallel RO-TENG devices. (c) Variation of voltage, current, and RMS current in the LPCMM driven by the parallel RO-TENG at an excitation frequency of 1 Hz. (d) Voltage curves for lithium batteries of different capacities at an excitation frequency of 1 Hz. (e) Comparison of the charging time between the parallel RO-TENG and LRH-250R, within a voltage range of 3 V to 3.5 V. (f) Voltage and current curves of lithium batteries with different capacities during the charging process, (i) 30 mA h, (ii) 40 mA h. (g) Voltage curves of a wireless Bluetooth sensor driven by the parallel RO-TENG.

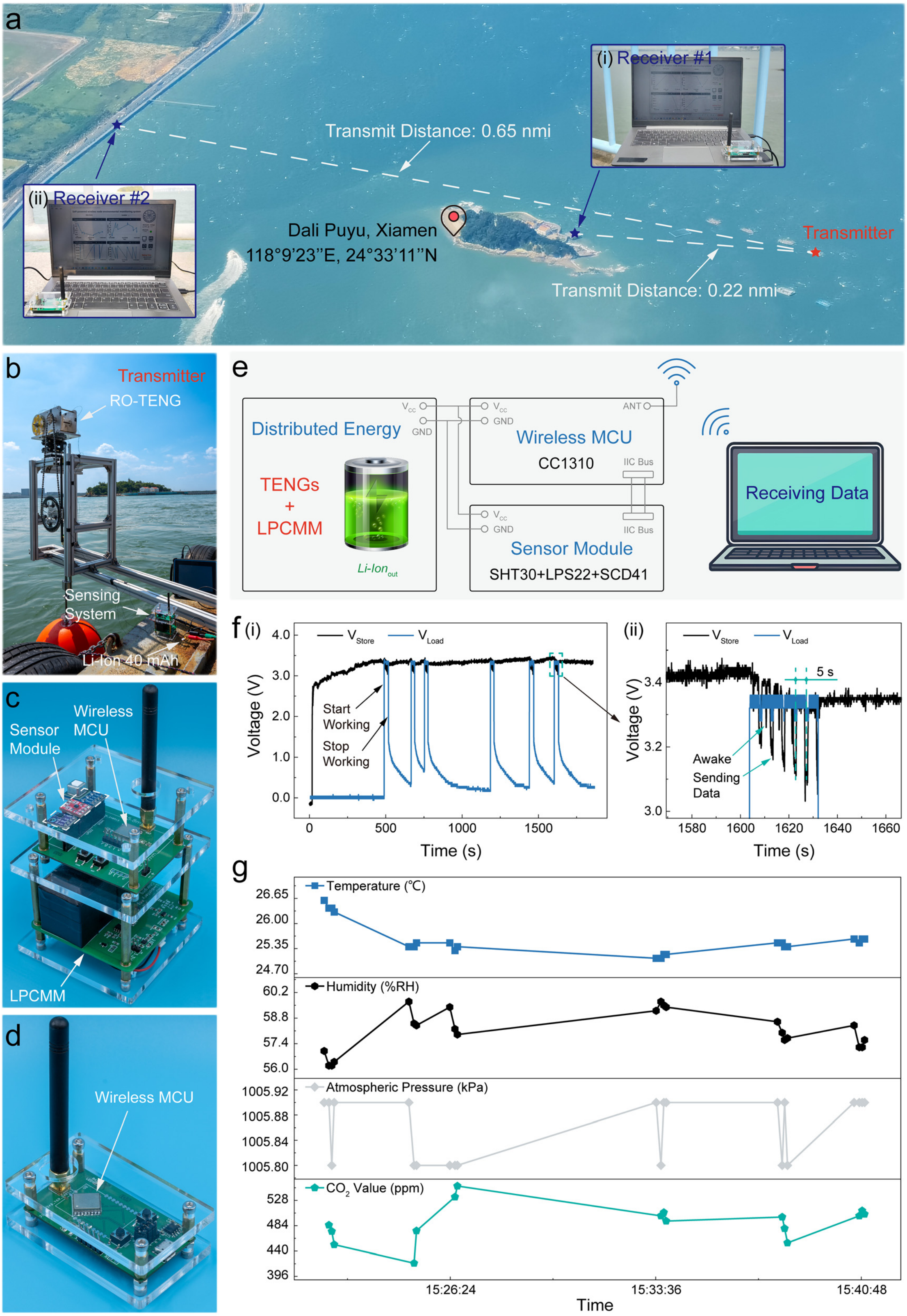

Fig. 5 Application demonstration of the RO-TENG in a real ocean environment. (a) Illustration of the transmission distance of self-powered environmental monitoring system, showing the location arrangement of the receiver (i), (ii). (b) Photograph of the RO-TENG-based transmitter in a real ocean environment. (c) Sketch of different functional parts of the transmitter. (d) Depiction of the various functional components of the receiver. (e) Architecture of the self-powered environmental monitoring system. (f) Voltage variation of the self-powered environmental monitoring system deployed under real ocean conditions. (g) Environmental data acquired from the monitoring system.

TENG. It takes approximately 8.2 minutes to charge the battery to 3.5 V under actual wave heights ranging from 0.1 m to 0.3 m. Once the lithium battery reaches this voltage, the wireless sensor node for environmental monitoring is activated. During the charging process, the battery's charging speed fluctuates intermittently due to the time-varying nature of the ocean environment. An enlarged view of the voltage profile from the sensor node is shown in Fig. 5(f)-(ii). Upon activation, the sensor node begins detecting and transmitting data at ambient temperature, humidity, atmospheric pressure, and CO_2 levels to the receiver. Thanks to the high energy density of the lithium battery, the sensor node can operate continuously for 30 s, transmitting environmental data to the receiver every 5 s. Fig. 5(g) and Fig. S28 (ESI†) present the environmental data received from the node on December 4th and October 9th, respectively (Movies S5 and S6 (ESI†)). Clearly, both experiments reliably detect and transmit environmental data, demonstrating that the entire system can operate stably and continuously over extended periods when deployed along the coast. This achievement marks a pioneering advancement in utilizing a fully TENG-based device for lithium battery energy storage under actual ocean conditions, elevating the TENG technology to a new level of large-scale application in marine environments.

Conclusions

In this work, a universal lithium battery energy storage strategy based on the RO-TENG in a real ocean environment was designed and proposed. The RO-TENG integrates multiple grating electrodes and the opposite-charge ternary electrification architecture compensation mechanism to efficiently harvest wave energy. Owing to this design, the RO-TENG can generate an RMS current density of 57.19 ± 0.23 mA m^{-2} Hz^{-1} and an average power density of 3.28 ± 0.07 W m^{-2} Hz^{-1} at a matching resistance of 200 kΩ, which are significantly higher than those reported in previous works. Meanwhile, after 48 612 960 cycles of stability testing, the RO-TENG demonstrates excellent durability, with an attenuation of only 10%. Subsequently, based on exceptional electrical performance, the LPCMM was designed. An RMS current density of 0.86 ± 0.02 A m^{-2} Hz^{-1} is generated by the LPCMM-integrated parallel RO-TENG, representing a 14-fold enhancement. Simultaneously, when charged by the RO-TENG operating at a frequency of 1 Hz for 1 h, the lithium battery capacity increases to approximately 12 mA h, indicating an improvement of over 20-times compared to that of direct charging by a TENG. And, it took 2.33 ± 0.05 h and 3.73 ± 0.14 h to fully charge lithium batteries with nominal capacities of 30 mA h and 40 mA h, respectively. Furthermore, the time required to fully charge the aforementioned lithium batteries using the RO-TENG with LPCMM is only 7.35% and 8.07% longer, respectively, compared to that achieved by a commercial method. Finally, a self-powered marine environmental monitoring system was demonstrated in a real ocean environment. Remote real-time wireless monitoring of temperature, humidity, atmospheric pressure, and CO_2 levels, over a maximum transmission distance of 0.65 nautical miles (1.2 km), was achieved under actual wave heights ranging from 0.1 m to 0.3 m. The results have validated the superiority of the lithium battery energy storage strategy based on the RO-TENG and demonstrated its potential as a distributed energy source for self-powered sensing nodes in marine IoT applications.

Experimental

Fabrication of the RO-TENG

The RO-TENG consists of a rotor and a stator. The rotor has an acrylic base for laser cutting, with a diameter of 110 mm and a thickness of 5 mm, respectively. The upper surface of the acrylic disk is symmetrically affixed to four circular weights of equal mass with a diameter of 24 mm, a thicknesses of 3.7 mm, and a weight of 10 g, respectively. The lower surface of the acrylic disk is coated with 60 fan-shaped PTFE films with a central angle of 3° and a thickness of 50 μm. The material and dimensions of the stator are the same as those of the rotor. The upper surface of the stator has 120 copper electrodes with a central angle of 3° and a thickness of 20 μm, and the copper electrodes are coated with a 50 μm-thick nylon film.

Measurement and characterization

A linear motor (LinMot-E1100, NTI AG, Switzerland) was utilized to simulate linear excitations, aiding in the evaluation of the output performance of the RO-TENG. The output voltage and charge of the RO-TENG were measured using an electrometer (6514, Keithley, USA), and output current of the RO-TENG was measured using an electrometer (SR570, Stanford SRS, USA). The surface structure of PTFE and Nylon was measured using an optical microscope (Ni-E, Nikon, Japan). The voltage and current of the lithium battery were measured using an oscillograph (STO1004, Micsig, China) and an electrometer (6514, Keithley, USA), respectively, during a series of experiments conducted in the actual marine environment. The variation curves of discharge voltage with capacity of lithium batteries with different capacities were measured using a commercial lithium battery test system (LRH-250R, keelrein, China).

Author contributions

Y. L. and W. G. conceived the idea. W. G. and Z. L. W. conducted the work and supervised the experiments. Y. L. and W. G. prepared the manuscript. Y. L. and W. L. designed and fabricated the device and performed the electrical measurements. C. P. and T. J. designed and conducted simulation experiment. C. P., T. J., A. L., D. Y., and J. X. helped for the electrical measurements and application demonstration. All the authors discussed the results and commented on the manuscript.

Data availability

The authors declare that the main data supporting the findings of this study are available within the article and its ESI.† Extra data are available from the corresponding authors on reasonable request.

Conflicts of interest

The authors declare no competing financial interest.

Acknowledgements

This work was supported by the National Nature Science Foundation of China (22175146, 22475182), the Fundamental Research Funds for the Central Universities of China (20720240140), and the ''111'' Project (B16029).

References

1 Z. Yuan, C. Wang, J. Xi, X. Han, J. Li, S.-T. Han, W. Gao and C. Pan, *ACS Energy Lett.*, 2021, **6**, 2809–2816.
2 S. Yang, C. Zhang, Z. Du, Y. Tu, X. Dai, Y. Huang, J. Fan, Z. Hong, T. Jiang and Z. L. Wang, *Adv. Energy Mater.*, 2024, **14**, 2304184.
3 Y. Wang, H. Du, H. Yang, Z. Xi, C. Zhao, Z. Qian, X. Chuai, X. Peng, H. Yu, Y. Zhang, X. Li, G. Hu, H. Wang and M. Xu, *Nat. Commun.*, 2024, **15**, 6834.
4 S. Yong, J. Wang, L. Yang, H. Wang, H. Luo, R. Liao and Z. L. Wang, *Adv. Energy Mater.*, 2021, **11**, 2101194.
5 Y. C. Pan, Z. Dai, H. Ma, J. Zheng, J. Leng, C. Xie, Y. Yuan, W. Yang, Y. Yalikun, X. Song, C. B. Han, C. Shang and Y. Yang, *Nat. Commun.*, 2024, **15**, 6133.
6 J. Luo, Z. Wang, L. Xu, A. C. Wang, K. Han, T. Jiang, Q. Lai, Y. Bai, W. Tang, F. R. Fan and Z. L. Wang, *Nat. Commun.*, 2019, **10**, 5147.
7 C. Zhang, Y. Liu, B. Zhang, O. Yang, W. Yuan, L. He, X. Wei, J. Wang and Z. L. Wang, *ACS Energy Lett.*, 2021, **6**, 1490–1499.
8 Y. Yu, Q. Gao, X. Zhang, D. Zhao, X. Xia, J. Wang, H. Li, Z. L. Wang and T. Cheng, *Energy Environ. Sci.*, 2023, **16**, 3932–3941.
9 J. Wang, X. Yu, D. Zhao, Y. Yu, Q. Gao, T. Cheng and Z. L. Wang, *Adv. Energy Mater.*, 2021, **11**, 2101356.
10 L. Long, W. Liu, Z. Wang, W. He, G. Li, Q. Tang, H. Guo, X. Pu, Y. Liu and C. Hu, *Nat. Commun.*, 2021, **12**, 4689.
11 D. Liu, C. Li, P. Chen, X. Zhao, W. Tang and Z. L. Wang, *Adv. Energy Mater.*, 2022, **13**, 2202691.
12 X. Fu, S. Xu, Y. Gao, X. Zhang, G. Liu, H. Zhou, Y. Lv, C. Zhang and Z. L. Wang, *ACS Energy Lett.*, 2021, **6**, 2343–2350.
13 R. K. Jain, J. Qin and R. Rajagopal, *Nat. Energy*, 2017, **2**, 17112.
14 H. Fu, X. Mei, D. Yurchenko, S. Zhou, S. Theodossiades, K. Nakano and E. M. Yeatman, *Joule*, 2021, **5**, 1074–1118.
15 J. Chen, Y. Huang, N. Zhang, H. Zou, R. Liu, C. Tao, X. Fan and Z. L. Wang, *Nat. Energy*, 2016, **1**, 16138.
16 H. S. Boudet, *Nat. Energy*, 2019, **4**, 446–455.
17 H. Wang, L. Xu, Y. Bai and Z. L. Wang, *Nat. Commun.*, 2020, **11**, 4203.
18 H. Qiu, H. Wang, L. Xu, M. Zheng and Z. L. Wang, *Energy Environ. Sci.*, 2023, **16**, 473–483.
19 X. Li, L. Xu, P. Lin, X. Yang, H. Wang, H. Qin and Z. L. Wang, *Energy Environ. Sci.*, 2023, **16**, 3040–3052.
20 H. Hong, X. Yang, H. Cui, D. Zheng, H. Wen, R. Huang, L. Liu, J. Duan and Q. Tang, *Energy Environ. Sci.*, 2022, **15**, 621–632.
21 Z. Deng, L. Xu, H. Qin, X. Li, J. Duan, B. Hou and Z. L. Wang, *Adv. Mater.*, 2022, **34**, 2205064.
22 B. Cao, P. Wang, P. Rui, X. Wei, Z. Wang, Y. Yang, X. Tu, C. Chen, Z. Wang, Z. Yang, T. Jiang, J. Cheng and Z. L. Wang, *Adv. Energy Mater.*, 2022, **12**, 2202627.
23 X. Zhao, H. Askari and J. Chen, *Joule*, 2021, **5**, 1391–1431.
24 W. Xu, H. Zheng, Y. Liu, X. Zhou, C. Zhang, Y. Song, X. Deng, M. Leung, Z. Yang, R. X. Xu, Z. L. Wang, X. C. Zeng and Z. Wang, *Nature*, 2020, **578**, 392–396.
25 Z. L. Wang, J. Chen and L. Lin, *Energy Environ. Sci.*, 2015, **8**, 2250–2282.
26 C. Rodrigues, D. Nunes, D. Clemente, N. Mathias, J. M. Correia, P. Rosa-Santos, F. Taveira-Pinto, T. Morais, A. Pereira and J. Ventura, *Energy Environ. Sci.*, 2020, **13**, 2657–2683.
27 Z. L. Wang, *Mater. Today*, 2022, **52**, 348–363.
28 F.-R. Fan, Z.-Q. Tian and Z. Lin Wang, *Nano Energy*, 2012, **1**, 328–334.
29 X. Liu, Z. Zhao, Y. Gao, Y. Nan, Y. Hu, Z. Guo, W. Qiao, J. Wang, L. Zhou, Z. L. Wang and J. Wang, *Energy Environ. Sci.*, 2024, **17**, 3819–3831.
30 R. Lei, Y. Shi, Y. Ding, J. Nie, S. Li, F. Wang, H. Zhai, X. Chen and Z. L. Wang, *Energy Environ. Sci.*, 2020, **13**, 2178–2190.
31 W. He, W. Liu, J. Chen, Z. Wang, Y. Liu, X. Pu, H. Yang, Q. Tang, H. Yang, H. Guo and C. Hu, *Nat. Commun.*, 2020, **11**, 4277.
32 Z. Guo, P. Yang, Z. Zhao, Y. Gao, J. Zhang, L. Zhou, J. Wang and Z. L. Wang, *Energy Environ. Sci.*, 2023, **16**, 5294–5304.
33 S. Fu, W. He, Q. Tang, Z. Wang, W. Liu, Q. Li, C. Shan, L. Long, C. Hu and H. Liu, *Adv. Mater.*, 2021, **34**, 2105882.
34 W. Yan, Y. Liu, P. Chen, L. N. Y. Cao, J. An, T. Jiang, W. Tang, B. Chen and Z. L. Wang, *Adv. Energy Mater.*, 2022, **12**, 2103677.
35 Z. Wang, Q. Tang, C. Shan, Y. Du, W. He, S. Fu, G. Li, A. Liu, W. Liu and C. Hu, *Energy Environ. Sci.*, 2021, **14**, 6627–6637.
36 Z. Wang, W. Liu, W. He, H. Guo, L. Long, Y. Xi, X. Wang, A. Liu and C. Hu, *Joule*, 2021, **5**, 441–455.
37 W. Liu, Z. Wang, G. Wang, Q. Zeng, W. He, L. Liu, X. Wang, Y. Xi, H. Guo, C. Hu and Z. L. Wang, *Nat. Commun.*, 2020, **11**, 1883.
38 Y. Dai, G. Liu, J. Cao, B. Fan, W. Zhou, Y. Li, J. Yang, M. Li, J. Zeng, Y. Chen, Z. L. Wang and C. Zhang, *Adv. Sci.*, 2024, **11**, 2404253.
39 P. Chen, Y. Luo, R. Cheng, S. Shu, J. An, A. Berbille, T. Jiang and Z. L. Wang, *Adv. Energy Mater.*, 2022, **12**, 2201813.
40 P. Chen, J. An, R. Cheng, S. Shu, A. Berbille, T. Jiang and Z. L. Wang, *Energy Environ. Sci.*, 2021, **14**, 4523–4532.

